JOURNAL OF
SYNCHROTRON
RADIATION

ISSN 1600-5775

Towards chemically neutral carbon cleaning processes: plasma cleaning of Ni, Rh and Al reflective optical coatings and thin Al filters for free-electron lasers and synchrotron beamline applications

Received 22 March 2018
Accepted 3 October 2018

Edited by M. Yabashi, RIKEN SPring-8 Center, Japan

Keywords: carbon contamination; FEL and synchrotron radiation beamline optics; free-electron lasers (FELs); plasma cleaning chemistry; inductively coupled plasma.

Harol Moreno Fernández,[a] Marco Zangrando,[b,c] Guillaume Sauthier,[d] Alejandro R. Goñi,[e,f] Vincent Carlino[g] and Eric Pellegrin[a]*

[a]Experiments Division, CELLS-ALBA, Carrer de la Llum 2-26, Cerdanyola del Valles, Barcelona E-08290, Spain, [b]Elettra-Sincrotrone Trieste, Strada Statale 14, km 163.5, Basovizza, I-34149 Trieste, Italy, [c]IOM-CNR, Strada Statale 14, km 163.5, Basovizza, I-34149 Trieste, Italy, [d]ICN2, Campus UAB, Bellaterra, Barcelona E-08193, Spain, [e]Institut de Ciència de Materials de Barcelona (ICMAB-CSIC), Campus UAB, Bellaterra, Barcelona E-08193, Spain, [f]ICREA, Passeig Lluís Companys 23, Barcelona E-08010, Spain, and [g]ibss Group Inc., Burlingame, CA 94010, USA.
*Correspondence e-mail: epellegrin@cells.es

The choice of a reflective optical coating or filter material has to be adapted to the intended field of application. This is mainly determined by the required photon energy range or by the required reflection angle. Among various materials, nickel and rhodium are common materials used as reflective coatings for (soft) X-ray mirrors. Similarly, aluminium is one of the most commonly used materials for extreme ultraviolet and soft X-ray transmission filters. However, both of these types of optics are subject to carbon contamination, which can be increasingly problematic for the operation of the high-performance free-electron laser and synchrotron beamlines. As an attempt to remove this type of contamination, an inductively coupled plasma source has been used in conjunction with $N_2/O_2/H_2$ and N_2/H_2 feedstock gas plasmas. Results from the chemical surface analysis of the above materials before and after plasma treatment using X-ray photoelectron spectroscopy are reported. It is concluded that a favorable combination of an N_2/H_2 plasma feedstock gas mixture leads to the best chemical surface preservation of Ni, Rh and Al while removing the carbon contamination. However, this feedstock gas mixture does not remove C contamination as rapidly as, for example, an $N_2/O_2/H_2$ plasma which induces the surface formation of NiO and NiOOH in Ni and RhOOH in Rh foils. As an applied case, the successful carbon removal from ultrathin Al filters previously used at the FERMI FEL1 using an N_2/H_2 plasma is demonstrated.

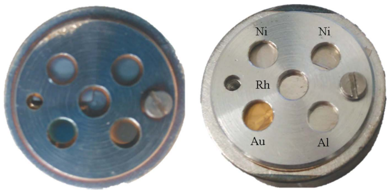

1. Introduction

Synchrotron radiation is an established powerful tool for a broad range of research in science and technology. The increase in synchrotron laboratories worldwide highlights the interest by commercial, educational and medical scientific research for obtaining analytical results that are only achievable using accelerator-based high-brilliance light sources. New generations of accelerator-based light sources with enhanced performance such as, for example, free-electron lasers (FELs), offer new possibilities for fundamental and applied research in the field of time-resolved and/or coherence-based experiments. In this context, one pressing practical requirement is to maintain the enhanced performance of these facilities, which includes maintaining reflective and transmission beamline optics as close as possible to their original/pristine state.

Rh and Ni (amongst others) are the most common optical coatings for synchrotron mirrors, due to their reflectance characteristics, where the material choice depends on the intended field of application and becomes an integral part of the beamline optics design. Aluminium is often used as a material for extreme ultraviolet (EUV) and soft X-ray filters due to its specific mechanical properties, thermal conductance and wide photon energy bandpass while blocking, among others, visible light.

However, reflective optics, as well as transmission filters, are subject to carbon contamination buildup, representing an increasingly serious problem for the operation of high-performance FEL beamlines. Previous publications have shown that it is possible to clean this carbon contamination (González Cuxart *et al.*, 2016; Pellegrin *et al.*, 2014; Moreno Fernández *et al.*, 2018; Graham *et al.*, 2002; Thedsakhulwong & Thowladda, 2008; Strein *et al.*, 2008; Eggenstein *et al.*, 2001; Hopf *et al.*, 2002; Pellegrin *et al.*, 2013) by using a different kind of plasma such as, for example, capacitively coupled plasma (CCP), inductively coupled plasma (ICP) and microwave plasma obtaining different results depending on the gas mixture, RF input power, frequencies and surfaces to be cleaned. Other alternative approaches include the use of oxygen gas bleeding in conjunction with the photon beam inside the UHV optics chambers (Warburton & Pianetta, 1992) or the *in situ* use of ozone generated *via* UV lamps (Yao-Leclerc *et al.*, 2011).

In the same vein and following previous studies (González Cuxart *et al.*, 2016; Pellegrin *et al.*, 2014; Moreno Fernández *et al.*, 2018), the ICP-type ibss model GV10x low-pressure plasma source together with $N_2/O_2/H_2$ and N_2/H_2 feedstock gases have been used to clean Ni, Rh and Al foil materials and ultrathin Al filters for EUV applications.

Using X-ray photoelectron spectroscopy (XPS), we report on changes regarding the surface chemistry of the above metals before and after the different plasma treatments. In addition, results from the successful carbon cleaning of ultrathin Al EUV filters used at the FERMI FEL1 (Allaria. *et al.*, 2012) are presented.

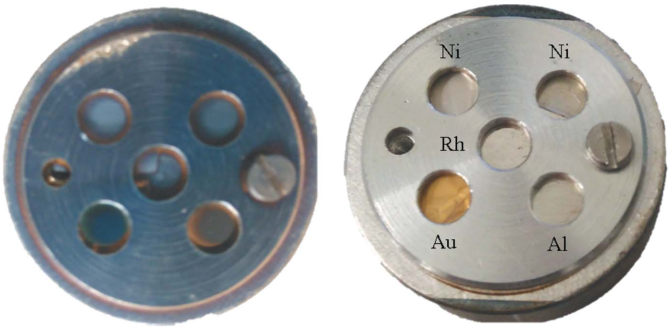

Figure 1
Ni, Rh, Al and Au metal foils of micrometric thickness installed on a common foil sample holder for plasma treatment. Left: metal foil sample holder before plasma cleaning, including a 50 nm a-C coating. Right: metal foil sample holder after plasma cleaning.

2. Experimental

2.1. Materials and cleaning test setup

A set of Ni, Rh and Al metal foils with micrometric thickness were contaminated with 50 nm of amorphous carbon (a-C) using electron beam deposition inside a commercial deposition setup together with high-purity polycrystalline graphitic carbon targets (Pellegrin *et al.*, 2014) for simulating a photon-beam induced carbon contamination (Fig. 1). In addition, self-supported ultrathin Al filters (Luxel Corporation, Friday Harbor, WA, USA) of 100 nm thickness were contaminated by exposure to the FEL photon beam at the FERMI FEL1. All samples were plasma cleaned in an ultrahigh vacuum (UHV) chamber (Fig. 2), where a 300 l s^{-1} turbomolecular pumping unit was installed in order to sustain a base pressure of 1.9×10^{-8} mbar. The plasma operating pressure was kept at 0.005 mbar (3.75 mTorr) for both $N_2(94\%)/O_2(4\%)/H_2(2\%)$ and $N_2(95\%)/H_2(5\%)$ feedstock gas mixtures supplied *via* commercial pre-mix gas bottles (provided by the Linde and Airgas companies, respectively). Both gases will be referred to as $N_2/O_2/H_2$ and N_2/H_2 hereafter. The plasma feedstock gas pressure was kept constant at 0.005 mbar, which gives the fastest carbon cleaning rates that can be obtained when cleaning carbon contamination on optical components in our setup with the above feedstock gases (González Cuxart *et al.*, 2016). The RF power applied to the RF coil of the ICP plasma source was maintained at 100 W (see the following subsection for further details on the plasma source).

2.2. Plasma source

The plasma source consists of a commercial ICP source (ibss model GV10x Downstream Asher, Burlingame, CA, USA; http://ibssgroup.com/products/gv10x/) operating at an

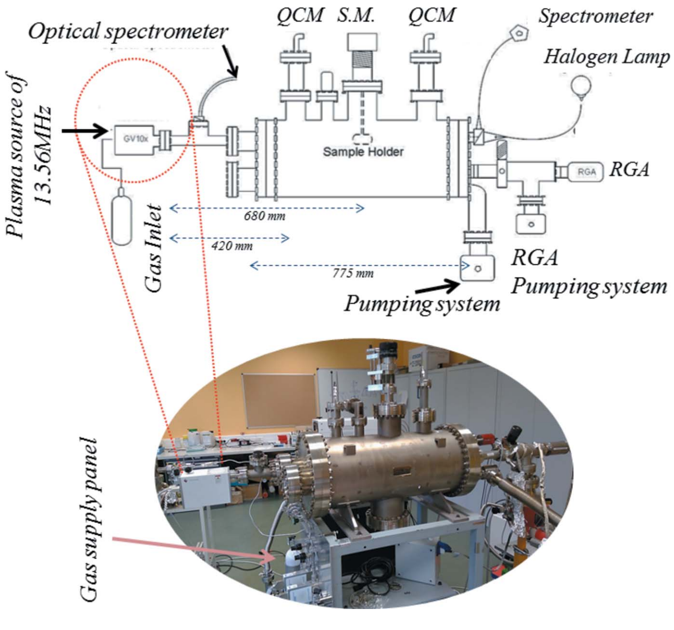

Figure 2
Schematic of the plasma cleaning chamber (QCM: quartz crystal monitor; S.M.: sample manipulator; RGA: residual gas analyzer).

RF frequency of 13.56 MHz. The plasma volume consists of a ceramic Al_2O_3 tube (5.5 inch length; 0.81 inch outer diameter) surrounded by an RF air coil with the gas supply and the plasma exhaust located at the ceramic tube back and front-end, respectively. The Downstream Asher operation principle allows for generating the plasma in a separate 'remote plasma' volume upstream of the UHV chamber including the plasma diagnostics and the optical objects to be cleaned. With the plasma source being localized outside the main chamber, the ionization of the different gases will only take place within the upstream plasma source. The a-C cleaning rate, as measured by the quartz crystal monitor closer to the plasma source (Fig. 2), was 7.2 Å min^{-1} and 2.5 Å min^{-1} for $N_2/O_2/H_2$ and N_2/H_2 plasma, respectively. This significant difference in terms of carbon cleaning rate is related to the small oxygen percentage in the former gas mixture. Differences in terms of cleaning rate were already observed in previous studies (González Cuxart *et al.*, 2016; Pellegrin *et al.*, 2014; Moreno Fernández *et al.*, 2018).

2.3. Characterization techniques

For the *in situ* detection of ionic species generated by the plasma, a differentially pumped residual gas analyzer (RGA) was installed at the remote end of the UHV chamber and an optical spectrometer was connected close to the GV10x plasma source exhaust to check the optical emission spectrum from the downstream plasma.

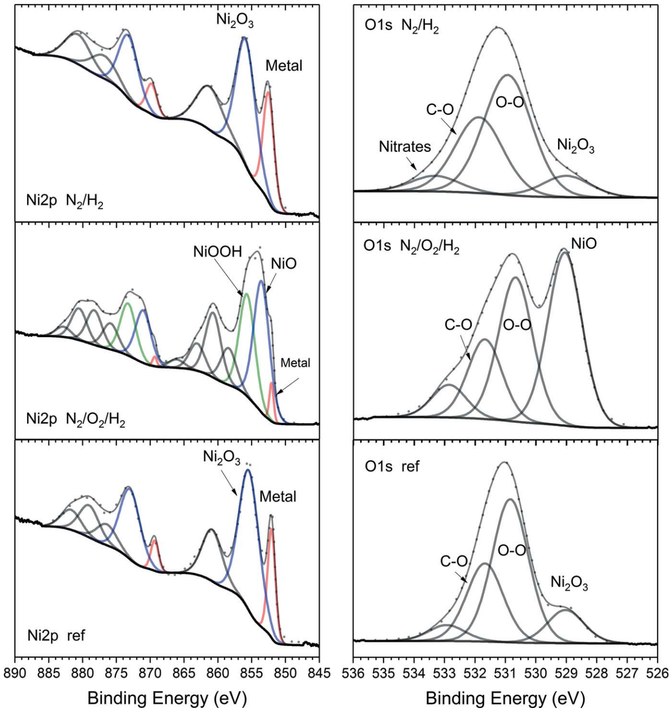

Figure 3
Ni 2*p* (left column) and O 1*s* (right column) XPS core-level spectra of Ni metal foils. Bottom row: pristine Ni reference sample. Center row: Ni foil after a-C contamination and subsequent $N_2/O_2/H_2$ plasma treatment. Top row: Ni foil after a-C contamination and subsequent N_2/H_2 plasma treatment.

Table 1
XPS core-level binding energies as obtained from the XPS spectra presented in Fig. 3 to Fig. 5.

XPS line	Reference foil BE (eV)	$N_2/O_2/H_2$ plasma BE (eV)	N_2/H_2 plasma BE (eV)
Ni metal foil			
Ni 2*p*	852.08 metal	852.1 metal	852.08 metal
	855.36 Ni_2O_3	853.58 NiO	855.41 Ni_2O_3
		855.71 NiO (+NiOOH)	
O 1*s*	529.02 Ni_2O_3	529.06 NiO	529.01 Ni2O3
	530.84 O—O	530.68 O—O	530.93 O—O
	531.67 O—H, O with C	531.68 O—H, O with C	531.88 O—H, O with C
	532.93	532.68	533.32 nitrates
Rh metal foil			
Rh 3*d*	307.04 metal	307.06 metal	307.05 metal
	307.60 Rh_2O_3	307.93 Rh_2O_3	308.27 Rh_2O_3
		309.59 RhOOH	
O 1*s*	529.52 Rh_2O_3	529.68 Rh_2O_3	530.23 Rh_2O_3
	531.59 carbonates	531.32 RhOOH	532.07 carbonates
		532.49 carbonates	
		534.35 absorbed H_2O	
Al metal foil			
Al 2*p*	72.53 metal $2p_{3/2}$		72.5 metal $2p_{3/2}$
	73.19 metal $2p_{1/2}$		73.1 metal $2p_{1/2}$
	75.47 Al_2O_3		75.41 Al_2O_3
O 1*s*	532.21 Al_2O_3		532.21 Al_2O_3
	533.45 C═O		533.52 C═O

Plasma-induced changes regarding the sample surface chemistry were analyzed offline by XPS using a SPECS Phoibos 150 electron energy analyzer (operated at 25 eV pass energy) in conjunction with a monochromated Al $K\alpha$ X-ray source (0.65 eV line widths at 1486.6 eV) for samples cleaned with $N_2/O_2/H_2$ plasma. On the other hand, a non-monochromated Al $K\alpha$ X-ray source has been used for the analysis of samples cleaned with N_2/H_2 plasma.

In addition, in order to contrast the chemical composition and allotropism of the carbon contamination coming on the Al EUV filters with respect to the deposited a-C, Raman spectroscopy was used to characterize these carbon contaminations using red laser light as an excitation source.

3. Results and discussion

3.1. Nickel XPS spectra

Fig. 3 shows the Ni 2*p* XPS spectrum for plasma-cleaned nickel foils using two different plasmas as compared with the pristine reference nickel foil (*i.e.* without any treatment). The binding energy (BE) values (Ni $2p_{3/2}$ and O 1*s*) as obtained from the different plasma treatments are reported in Table 1. After the cleaning process using N_2/H_2 plasma, no changes were observed regarding the Ni chemical surface state in both the native oxide surface layer as well as the Ni metal foil bulk, unlike expectations from previous studies (Pellegrin *et al.*, 2014), where hydrogen-based Ar/H_2 plasma had resulted in a significant reduction of the native Ni_2O_3 surface layer of the Ni foil.

In addition, as the intensity ratio between the Ni $2p_{3/2}$ lines for both Ni in Ni_2O_3 and in Ni metal remains unchanged, the thickness of the former native oxide layer appears to be unchanged. Regarding the O 1*s* XPS core-level data, the peak corresponding to Ni_2O_3 for the plasma-treated foil appears to be not as well defined as in the case of the Ni reference foil, most probably due to the non-monochromated Al *Kα* source used in the former case.

However, when using the $N_2/O_2/H_2$ plasma the Ni $2p_{3/2}$ spectrum shows a significant change towards a more complex structure with intense satellite lines at higher binding energies corresponding to the $\underline{c}d^8$ and $\underline{c}d^9\underline{L}$ plus the $\underline{c}d^{10}\underline{L}^2$ XPS final states, respectively. The Ni $2p_{3/2}$ line gives two different species at BE values of 853.58 and 855.71 eV compared with the Ni reference foil, apparently induced by the $N_2/O_2/H_2$ plasma treatment now including a small oxygen concentration. On the basis of their BEs, we assign these peaks to NiO and NiOOH, respectively, which is in agreement with previous studies (Biesinger *et al.*, 2012; see also http://www.xpsfitting.com/). The O 1*s* XPS spectrum gives four different peaks for all samples, although the spectrum from $N_2/O_2/H_2$ plasma-treated foil shows appreciable variations. Taking into account these changes, these O 1*s* spectral features can be assigned to different species and the associated BE positions are as follows: 529.06, 530.68 and 531.68 eV for NiO, O—O and C—O, respectively.

3.2. Rhodium XPS spectra

Fig. 4 shows the Rh 3*d* XPS spectra for the a-C contaminated and subsequently plasma-cleaned rhodium metal foils with two different plasmas as compared with a pristine reference rhodium foil (*i.e.* without any treatment). In the case of rhodium, we observe a similar behavior as in the case of nickel after N_2/H_2 plasma treatment, where chemical changes could not be observed in contrast to prior expectations based on previous studies. The peak position attributed to Rh_2O_3 oxide is shifted by 0.67 eV to higher BE in comparison with the Rh_2O_3 oxide from the reference foil (due to the lack of spectral features that would allow for a better fitting).

The reference Rh 3*d* spectra were fitted with two main peaks at binding energies of Rh $3d_{5/2}$ at 307.04 and 307.6 eV for metallic Rh and Rh_2O_3, respectively. The BEs of Rh metal and Rh_2O_3 oxide after the N_2/H_2 plasma treatment are in fair agreement with the values obtained by Kibis *et al.* (2016) for metallic Rh^0 and Rh^{3+} in Rh_2O_3, respectively, where peak positions at 307.3 and 308.2 eV, respectively, were obtained. As in the case of the N_2/H_2 plasma-treated Ni foil (Fig. 3, top row), the N_2/H_2 plasma-treated Rh foil exhibits slightly broader spectral lines due to the use of a non-monochromated Al *Kα* source.

After the $N_2/O_2/H_2$ plasma treatment, a clearly enhanced oxidation of the Rh foil can be observed from the increase of the Rh_2O_3-related $Rh_{5/2}$ peak at 307.93 eV BE (Fig. 4). The O 1*s* spectrum now shows four features: the peak formerly observed on the Rh reference foil as well as the N_2/H_2 plasma-treated Rh foil at 529.68 eV, plus additional peaks at 531.32, 532.49 and 534.35 eV BE. We attribute those additional peaks to Rh_2O_3, rhodium hydroxide groups (Kibis *et al.*, 2016; Tolia *et al.*, 1994; see also https://xpssimplified.com/elements/aluminium.php), carbonates and adsorbed H_2O. In this context, we associate the Rh $3d_{5/2}$ peak at 309.59 eV with the rhodium hydroxide group.

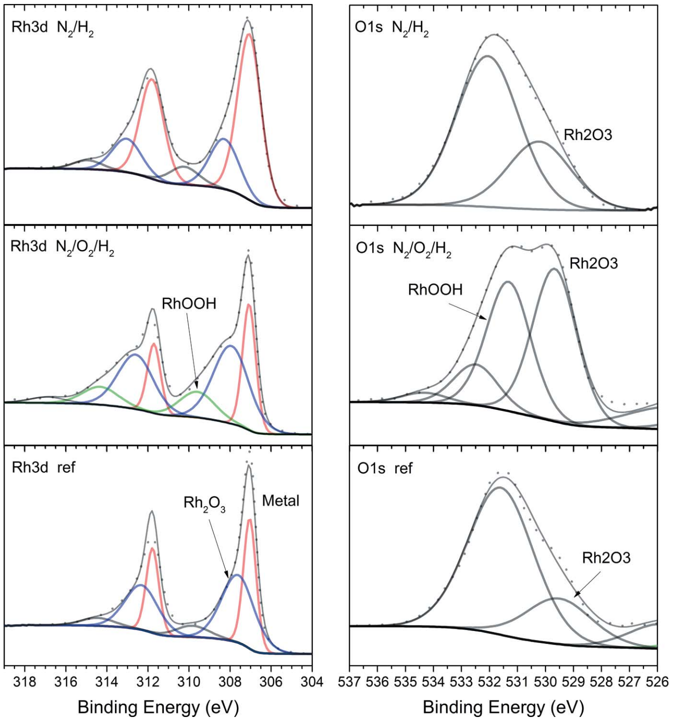

Figure 4

Rh 3*d* (left column) and O 1*s* (right column) XPS core-level spectra of Rh metal foils. Bottom row: pristine Rh metal reference sample. Center row: Rh foil after a-C contamination and subsequent $N_2/O_2/H_2$ plasma treatment. Top row: Rh foil after a-C contamination and subsequent N_2/H_2 plasma treatment.

In contrast to the previous study by Kibis *et al.* (2016), where RhO_2 peaks were found after plasma sputtering and characterized in terms of an additional O 1*s* line at 530.6 eV BE, we could not detect such a feature at this BE position in our O 1*s* XPS spectra. Nevertheless, the XPS data on RhO_2 are somewhat contradictory due to the fact that the $Rh^{4+}O_2$ in the $Rh_{5/2}$ core-level line has been reported to be in the range 309–310 eV, which in the case of our $N_2/O_2/H_2$ plasma treatment corresponds to a peak position at 309.59 eV. In that sense, we attribute the O 1*s* line at 531.32 eV and the Rh $3d_{5/2}$ line at 309.59 eV to Rh^{4+}/Rh^{3+}-based rhodium oxyhydroxide species (see Table 1).

3.3. Aluminium XPS spectra

Taking into account the results from the previous cleaning processes, where besides the expected significant a-C contamination removal only the N_2/H_2 plasma appears to leave the metal surface chemistry unchanged, we thus only performed a N_2/H_2 plasma cleaning process on the Al foils. In this way we avoid a further oxidation of the Al foil surface beyond the native Al_2O_3 layer, together with a possible mechanical destabilization *via* the formation of that brittle oxide. The detailed Al 2*p* and O 1*s* core-level spectra are shown in Fig. 5, for Al metal foils before and after a-C contamination plus subsequent N_2/H_2 plasma treatment. In both cases the metal peaks corresponding to the Al $2p_{3/2}$ and $2p_{1/2}$ core-level lines can be seen at 72.53 eV and 73.19 eV BE, respectively, while the peak at 75.47 eV is related to the Al_2O_3 surface layer.

These Al 2*p* spectral features are in good agreement with values found in the standard web-based XPS literature (https://xpssimplified.com/elements/aluminium.php) for Al oxide on Al foil. However, in contrast to values reported in the literature (Latsunskyi *et al.*, 2015; Zähr *et al.*, 2012), none of our XPS data on oxide surface layers show an O 1*s* peak in the typical oxide region between 529 and 530 eV; moreover, the values obtained are shifted by ~1 eV from values found in the literature. The O 1*s* peak is relatively broad and symmetric; its deconvolution shows two components for the reference foil as well as for the plasma-treated Al foil with BEs of 532.21 and 533.45 eV. In the case of plasma-treated Al foil, a clear difference in the ratios of these two components can be seen. The peak at 532.21 eV BE related to Al_2O_3 increases after plasma treatment, indicating an increase of the oxide thickness. This assumption can easily be corroborated using the calculations of the type developed by Strohmeier (1990), yielding a small increase of the oxide thickness from 4.6 to 4.8 nm thickness. From the O 1*s* spectra in Fig. 5, it can also be seen that there is a decrease of the carbon–oxygen C═O-related line at 533.45 eV BE that we attribute to the presence of physisorbed adventitious carbonyl groups on the surface of the Al reference sample. It should be noted in this context that all reference samples were measured by XPS ‘as received’.

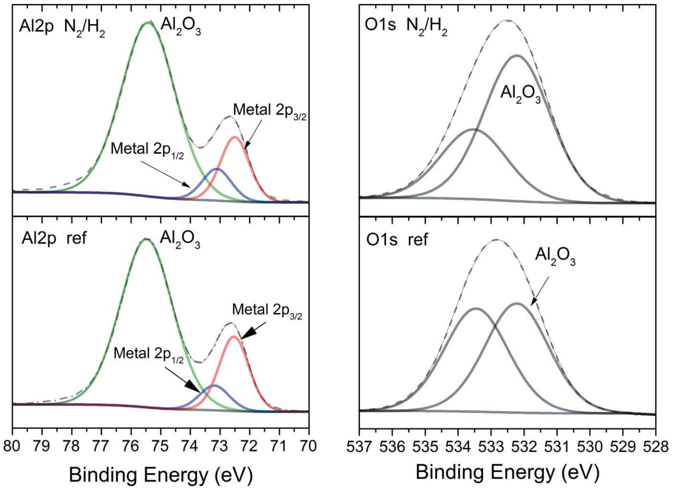

Figure 5
Al 2*p* (left column) and O 1*s* (right column) XPS core-level spectra of Al metal foils. Bottom row: pristine Al reference sample. Top row: Al foil after a-C contamination and subsequent N_2/H_2 plasma treatment.

3.4. Al EUV filter cleaning

Taking into account the above results regarding the performance of the N_2/H_2 plasma and especially its interesting feature on the preservation of the original surface chemistry of the plasma-processed metal foils, one can conclude that this process would be sufficiently safe for the carbon contamination cleaning of the corresponding thin Al filter foils. Here, besides restoring the original optical performance of the pure Al metal filter material, the preservation of the mechanical integrity of these devices is of prime importance. Thus, avoiding an increase of the native Al_2O_3 surface layer thickness is of importance for both the optical as well as the mechanical performance of these self-supported ultrathin Al filter foils.

We have thus performed a N_2/H_2 plasma cleaning on a set of Al EUV foil filters that have been exposed for roughly 500 operation hours to the pulsed high-brilliance photon beam of the FERMI FEL1 in the photon energy range from 20 to 65 eV. The results from the above plasma cleaning process are shown in Fig. 6. As can be seen, a successful carbon removal was obtained on the considerably more carbon-contaminated filter upstream side. An additional interesting feature is that the carbon-contaminated Al filter foils exhibit a wrinkled appearance at the position of the carbon footprint (Fig. 6*a*). As can be seen from Fig. 6(*b*) after plasma cleaning, the cleaned filter surfaces no longer show any wrinkles. We conclude from this that the foil wrinkles do result from the fact that the carbon layer is deposited onto the Al metal at elevated temperatures during the photon beam exposure. After cooling down, the difference in linear thermal coefficients between these two materials [aluminium: 21 × 10^{-6} to 25 × 10^{-6} m (m K)$^{-1}$; graphite: 4 × 10^{-6} to 8 × 10^{-6} m (m K)$^{-1}$; RT values] results in the observed formation

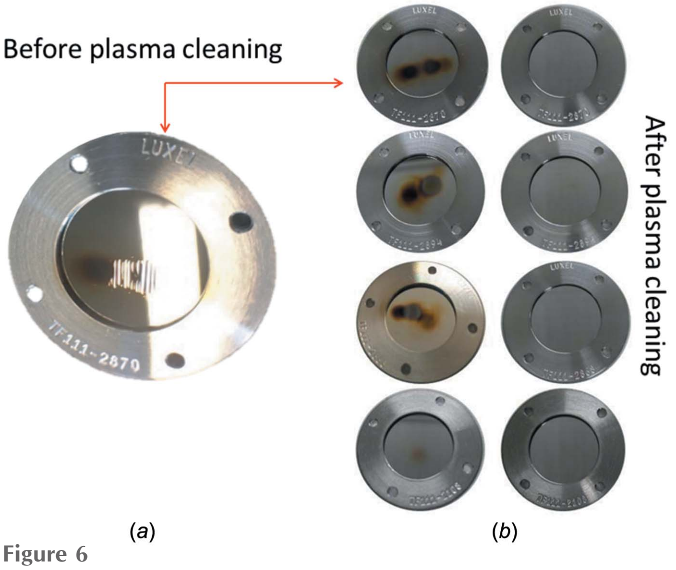

Figure 6
(*a*) Upstream side of a self-sustained Al filter foil with 100 nm thickness used at the FERMI FEL1. The foil wrinkles within the carbon footprint induced by the deposition of the carbon layer at elevated foil temperatures can be clearly distinguished. (*b*) Upstream side of four different self-sustained Al filter foils with 100 nm foil thickness used at the FERMI FEL1 before (left column) and after (right column) N_2/H_2 plasma treatment. Several photon beam-induced carbon footprints per filter foil can clearly be distinguished from the images in the left-hand side column.

of wrinkles associated with mechanical stress at the carbon/Al interface. Thus, the removal of the carbon footprint simultaneously does remove the observed wrinkles within the Al filter foils, becoming stress-free again.

3.5. Carbon contamination and plasma cleaning mechanism

Raman spectroscopy was used to characterize the different carbon contamination on the various samples in order to establish a comparison between the carbon cleaning characteristic of the carbon deposited on the EUV filters and the carbon deposited on the metal foils. Fig. 7 shows the Raman spectra for the different carbon contamination, plus a carbon contamination from a gold-coated mirror used at a soft X-ray bending magnet beamline at the former Synchrotron Radiation Center (SRC). The most intense contamination corresponds to the upstream side of the EUV filter as can be seen from Fig. 7, showing two characteristic carbon-related peaks denoted as D (1378 cm^{-1}) and G (1542 cm^{-1}). Although these peaks can be distinguished, the carbon content is related to amorphous carbon (a-C) with little graphitic ordering; the same accounts for the contamination from the back side and the SRC carbon contamination.

Note that in graphite the G mode is at 1581 cm^{-1} involving the in-plane bond-stretching motion of C sp^2 atom pairs, while the D peak lies around 1355 cm^{-1} and is known as a defect mode. This mode is forbidden in perfect graphite and only becomes active in the presence of disorder (Ferrari & Robertson, 2000). In this context it is possible to deduce that the carbon contamination on the Al filter foils also does not show a purely graphitic behavior, as it rather consists of a mixture of sp^2 and sp^3 hybridized carbon consisting of broad and smooth Raman spectral features. Hence, the broadening of the Raman bands and the high intensity of the D peak relative to the G peak indicate a low graphitic content in the carbon contamination footprint (Moreno *et al.*, 2014). Summarizing, there is an overall chemical and structural similarity between the a-C deposits from both the SRC bending-magnet source and the FERMI FEL1 free-electron laser source but with a variance from the pure amorphous character of the carbon layer as generated by the e-beam deposition process.

By using the differentially pumped RGA within our experimental setup (see Fig. 2), we could confirm the formation of NH_3 species within the N_2/H_2 plasma. Fig. 8 shows the RGA time trend from the N_2/H_2 plasma cleaning process of the EUV Al foil filters. Previous studies describe ammonia formation in this type of plasma either by the adsorption of excited N_2 molecules and N_2^+ ions, followed by their dissociation at the stainless steel chamber inside walls and then recombining with atomic hydrogen from the gas phase or, alternatively, by the direct absorption of atomic N and H plasma species instead of dissociative adsorption (Carrasco *et al.*, 2011).

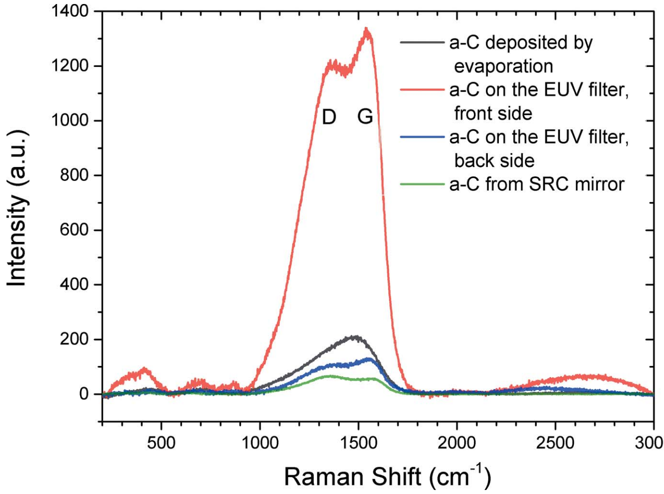

Figure 7
Raman spectra from different carbon contamination. Red solid line: carbon footprint on EUV Al filter foil upstream side. Black solid line: a-C thin film from e-beam carbon deposition. Blue solid line: carbon footprint on EUV Al filter foil downstream side. Green solid line: carbon footprint on Au-coated from SRC soft X-ray beamline.

Therefore, we tentatively attribute the carbon cleaning process mainly to the formation of ammonia within the N_2/H_2 plasma, assuming that NH_3 will reduce the amorphous sp^2/sp^3 carbon within the solid-state contamination layer and thus resulting in the subsequent formation of volatile C_xH_y hydrocarbon molecules. As for plasma processes in general, the carbon cleaning rate thereby not only depends on the total

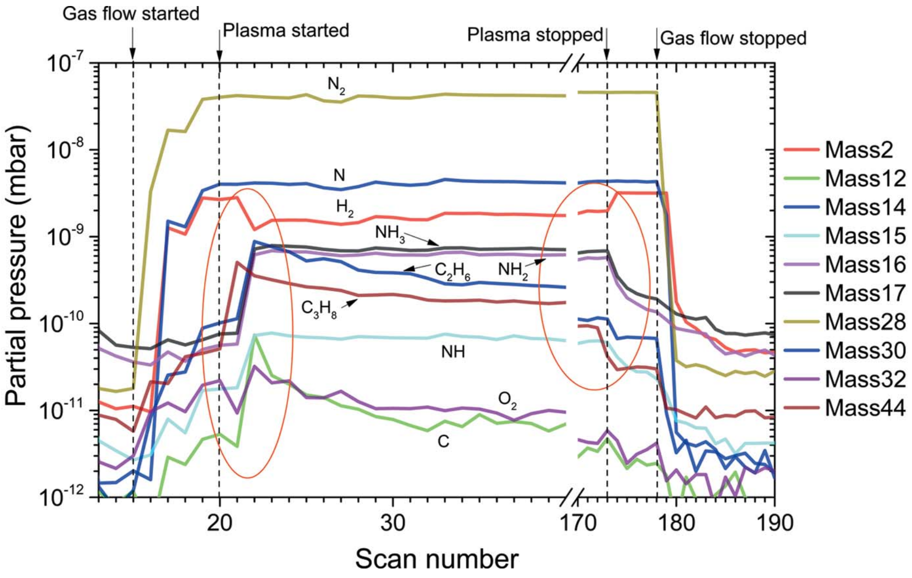

Figure 8
RGA time trend from the N_2/H_2 plasma during the plasma cleaning of the EUV Al foil filters. The complete time span of the RGA trend plot corresponds to about 4 h and 50 minutes (*i.e.* roughly 90 s per scan number increment).

pressure (*i.e. via* the corresponding mean free path lengths of the reactive plasmas species) but obviously also on the ammonia production rate/concentration within the plasma as a function of the applied RF power as could be shown in one of our previous studies on oxygen- as well as hydrogen-based plasma (González Cuxart *et al.*, 2016).

According to the above considerations and as can be seen from the experimental partial pressure RGA data in Fig. 8, the ignition of the RF plasma (*i.e.* at the time of RGA scan number 20) results in the formation of NH_3 (mass 17) species together with corresponding NH_2 and NH fractioning products generated at the RGA ionization unit (*i.e.* masses 16 and 15, respectively), which all occur at the expense of the observed H_2 partial pressure. In the same vein, the above process is inverted in time once the RF plasma is stopped (*i.e.* at the time of RGA scan number 173) where the H_2 partial pressure increases while the NH_z partial pressures decrease.

As can also be seen from Fig. 8 and regarding the carbon removal process, the gaseous C_xH_y products from the above reaction between the carbon contamination layer and the NH_z species show the same time dependence as a function of plasma operation time as compared with the ethane (mass 30) and propane (mass 44) time trends. The latter two time trends appear and disappear with the plasma being on or off, respectively (see the regions highlighted by red ellipses), thus demonstrating the direct coupling between the plasma operation and the carbon conversion into gaseous C_xH_y products. From the decrease of the ethane and propane time trends during plasma operation, one can derive the depletion of carbon species within the plasma cleaning chamber as a function of the plasma operation time.

Several previous studies (Ferreira *et al.*, 2009; Drenik *et al.*, 2016) have reported on the removal of carbon-based residues (such as, for example, a-C:H) from vacuum chambers as used in the ITER fusion reactor project using non-oxidizing plasma with either pure NH_3- or $N_2(37\%)/H_2(63\%)$-based feedstock gas mixtures. While these studies were working with distinctly higher hydrogen concentrations as compared with our present study, the results are also indicating carbon cleaning mechanisms based on NH_z species as the main chemically active cleaning agents. However, the observed volatile reaction products were HCN (mass 27) and C_2H_2 (mass 26) that are incompatible with our present RGA mass spectra. We thus tentatively ascribe these different reaction products to differences in the feedstock gas mixtures used, with our present study operating in the low hydrogen concentration regime regarding the plasma feedstock gas composition.

4. Conclusions

Summarizing, we conclude that a favorable combination of a $N_2(95\%)/H_2(5\%)$ plasma feedstock gas mixture leads to the best chemical surface preservation results for non-inert metal optical coatings such as Ni, Rh and Al together with the removal of carbon contamination and including an acceptable carbon cleaning rate. However, the above feedstock gas mixture does not remove carbon contamination as fast as, for example, a $N_2(94\%)/O_2(4\%)/H_2(2\%)$ plasma which, on the other hand, induces the surface formation of NiO and NiOOH in Ni and RhOOH in Rh foils. Thus, the application of a specific gas mixture for low-pressure RF plasma has to be considered on the background of the beamline optics requirements. It should be emphasized in this context that the above metal surface preservation has been demonstrated for the specific cases of Rh, Ni and Al and cannot necessarily be transferred directly to other metals without prior testing.

As an application of the above $N_2(95\%)/H_2(5\%)$ plasma, we demonstrated a first efficient *ex situ* carbon cleaning process of self-supported thin Al foil optical filters (100 nm thickness) as a specific case study within the field of transmission optics for FEL application in the EUV photon energy range. As an interesting side effect, macroscopic wrinkles in the Al foil located within the carbon footprint were removed simultaneously.

Acknowledgements

We acknowledge the expert assistance by M. Dominguez Escalante (UPC, Barcelona) for the XPS measurements as well as by F. J. Belarre Triviño (ICN2, Bellatera) for the carbon deposition process. The authors declare no competing financial interest.

Funding information

The following funding is acknowledged: Generalitat de Catalunya, Departament d'Empresa i Coneixement (Dossier No. 2014 DI 037 to HAMF).

References

Allaria. *et al.* (2012). *Nat. Photon.* **6**, 699–704.
Biesinger, L. W., Lau, A. R., Gerson, A. R. & Smart, R. St C. (2012). *Phys. Chem. Chem. Phys.* **14**, 2434–2442.
Carrasco, M., Jiménez-Redondo, M., Tanarro, I. & Herrero, V. (2011). *Phys. Chem. Chem. Phys.* **13**, 19561–19572.
Drenik, A., Mourkas, R., Zaplotnik, G., Primc, M., Mozetič, P., Panjan, D., Alegre, D. & Tabarés, F. L. (2016). *J. Nucl. Mater.* **475**, 237–242.
Eggenstein, F., Senf, F., Zeschke, T. & Gudat, W. (2001). *Nucl. Instrum. Methods Phys. Res. A*, **325**, 467–468.
Ferrari, A. C. & Robertson, J. (2000). *Phys. Rev. B*, **61**, 14095–14107.
Ferreira, F. L., Tabarés, D. & Tafalla, D. (2009). *J. Nucl. Mater.* **390–391**, 593–596.
González Cuxart, M., Reyes-Herrera, J., Šics, I., Goñi, H., Fernandez, H. M., Carlino, V. & Pellegrin, E. (2016). *Appl. Surf. Sci.* **362**, 448–458.
Graham, C., Steinhaus, M., Clift, L. & Klebanoff, L. (2002). *J. Vac. Sci. Technol. B*, **20**, 2393.
Hopf, C., von Keudell, A. & Jacob, W. (2002). *Nucl. Fusion*, **42**, L27–L30.
Kibis, A., Stadnichenko, S., Koscheev, V., Zaikovskii, V. I. & Boronin, A. (2016). *J. Phys. Chem. C*, **120**, 19142–19150.
Latsunskyi, I., Kempinski, M., Jancelewicz, M., Zaleski, K., Jurga, S. & Smyntyna, V. (2015). *Vacuum*, **113**, 52–58.
Moreno, S., Hussain, R., Amade, R. & Bertran, E. (2014). *Mater. Res. Expr.* **1**, 035050.
Moreno Fernández, H., Rogler, G., Sauthier, M., Thomasset, R., Dietsch, V., Carlino, E. & Pellegrin, E. (2018). *Sci. Rep.* **8**, 1293.

Pellegrin, E., Sics, I., Pérez Sempere, C., Reyes Herrera, J. & Carlino, V. (2013). *Proc. SPIE*, **8777**, 8777OP.

Pellegrin, E., Šics, I., Reyes-Herrera, J., Perez Sempere, C., Lopez Alcolea, J. J., Langlois, M., Fernandez Rodriguez, J. & Carlino, V. (2014). *J. Synchrotron Rad.* **21**, 300–314.

Strein, D., Allred, D. & Linford, M. (2008). *Microsc. Microanal.* **14**, 818–819.

Strohmeier, B. R. (1990). *Surf. Interface Anal.* **15**, 51–56.

Thedsakhulwong, A. & Thowladda, W. (2008). *J. Metals Mater. Miner.* **18**, 137–141.

Tolia, R., Smiley, W., Delgass, C., Takoudis, C. G. & Weaver, M. (1994). *J. Catal.* **150**, 56–70.

Warburton, P. & Pianetta, P. (1992). *Nucl. Instrum. Methods Phys. Res. A*, **319**, 240–243.

Yao-Leclerc, S., Brochet, C., Chauvet, C., De Oliveira, N., Duval, J.-F., Gil, S., Kubsky, B., Lagarde, L., Nahon, F., Nicolas, M., Silly, F., Sirotti, M. & Thomasset, M. (2011). *Proc. SPIE*, **8077**, 807712.

Zähr, J., Oswald, S., Türpe, M., Ullrich, H. J. & Füssel, U. (2012). *Vacuum*, **86**, 1216–1219.